Integrated effect of thermal ageing and low flux irradiation on microstructural evolution of the ferrite of welded austenitic stainless steels

Downloaded from: https://research.chalmers.se, 2025-07-03 03:02 UTC

Citation for the original published paper (version of record):
Lindgren, K., Bjurman, M., Efsing, P. et al (2021). Integrated effect of thermal ageing and low flux irradiation on microstructural evolution of
the ferrite of welded austenitic stainless steels. Journal of Nuclear Materials, 551.
http://dx.doi.org/10.1016/j.jnucmat.2021.152967

N.B. When citing this work, cite the original published paper.

research.chalmers.se offers the possibility of retrieving research publications produced at Chalmers University of Technology. It covers all kind of research output: articles, dissertations, conference papers, reports etc. since 2004. research.chalmers.se is administrated and maintained by Chalmers Library

(article starts on next page)

Journal of Nuclear Materials 551 (2021) 152967

Contents lists available at ScienceDirect

Journal of Nuclear Materials

journal homepage: www.elsevier.com/locate/jnucmat

Integrated effect of thermal ageing and low flux irradiation on microstructural evolution of the ferrite of welded austenitic stainless steels

K. Lindgren[a,*], M. Bjurman[b,c], P. Efsing[b,d], M. Thuvander[a]

[a] Chalmers University of Technology, Göteborg, Sweden
[b] Royal Institute of Technology (KTH), Stockholm, Sweden
[c] Studsvik Nuclear AB, Nyköping, Sweden
[d] Ringhals AB, Väröbacka, Sweden

ARTICLE INFO

Article history:
Received 13 November 2020
Revised 25 February 2021
Accepted 25 March 2021
Available online 28 March 2021

Keywords:
Spinodal decomposition
Thermal aging
G-phase
Atom probe tomography
Neutron irradiation
Austenitic welds
Delta ferrite

ABSTRACT

With the purpose to quantify microstructural changes with respect to ageing degradation, the microstructure of aged type 308 stainless steel welds with a ferrite content of 5-7% has been analysed using atom probe tomography. The weld metal of the core barrel of a decommissioned light water reactor, irradiated during operation of the reactor to 0.1 dpa, 1 dpa and 2 dpa at 280-285°C (231,000 h), are compared to two similar thermally aged welds. In the ferrite of the irradiated welds, there is spinodal decomposition into Cr-rich α' and Fe-rich α, with a similar degree of decomposition for all investigated doses, amplitudes of 21-26% and wavelengths between 6 and 9 nm. The ferrite of the thermally aged material showed evidence of decomposition when aged at 325°C (an amplitude of 13-14% and wavelength of 5 nm), but not when aged at 291°C, thus the irradiation significantly increases the rate of spinodal decomposition. There is G-phase ($Ni_{16}Si_7Mn_6$) precipitation in the ferrite of all the weld metals except the one that was thermally aged at the lowest temperature. After irradiation to 1 and 2 dpa, the G-phase is considerably more well developed than after 0.1 dpa or thermal ageing.

© 2021 The Authors. Published by Elsevier B.V.
This is an open access article under the CC BY license (http://creativecommons.org/licenses/by/4.0/)

1. Introduction

Austenitic stainless steels are commonly used in many components and structures of nuclear power plants due to their good weldability and corrosion properties. One example of such an area is the internal components of the reactor surrounding the nuclear core, providing core stability and cooling water guidance. During service, the internals are affected by the operating temperature (around 290-320°C in a typical pressurized water reactor) and neutron irradiation inside the reactor, resulting in a degradation of the mechanical properties. This can be visualized as an embrittlement of the material as the process progresses. Austenitic welds and castings typically contain some 4-15% and 10-30% of (delta) ferrite, respectively, to avoid solidification cracking [1–4].

The microstructural changes occurring in the material leading to degradation appear on the nanometre scale. In ferrite, spinodal decomposition into a Cr-depleted α and a Cr-enriched α' phase and G-phase formation in the region between the two phases have been observed to take place in reactor relevant environments [5]. G-phase has a nominal composition of $Ni_{16}Si_7Mn_6$ and a lattice parameter four times larger than that of ferrite [6–8]. However, other metallic elements (such as Cr, Fe, Ti, Mo) can substitute Ni and Mn [5,9]. During spinodal decomposition, Ni is rejected from the Cr-rich α' phase, whereas Si is rejected from the Fe-rich α phase, thus G-phase nucleates at the α/α' boundary.

The effect of thermal ageing on spinodal decomposition has been studied in both model alloys and in commercial steels [5,10–15]. A number of studies surveying the effect of irradiation on spinodal decomposition have also been peformed [16–19]. It is a common procedure to accelerate the ageing by subjecting the material to elevated temperatures or higher neutron flux, or to use ion irradiation to simulate neutron irradiation. However, relevant temperatures for accelerated ageing and subsequent validity of results is often questioned [20]. Furthermore, where combinations of thermal ageing and neutron irradiation are tested, ageing by increased temperature or irradiation are often applied in sequence, excluding any possible synergetic interactions. The validity of the results then has to be transferred to the actual conditions of the components,

* Corresponding author.
E-mail address: kristina.lindgren@chalmers.se (K. Lindgren).

https://doi.org/10.1016/j.jnucmat.2021.152967
0022-3115/© 2021 The Authors. Published by Elsevier B.V. This is an open access article under the CC BY license (http://creativecommons.org/licenses/by/4.0/)

Table 1
Investigated materials. CB stands for core barrel, CL for cross-over leg and HL for hot leg.

Namej	Dose (dpa)	Temperature (°C)	Time (h)
CB-0.1	0.1	280-285	231,000
CB-1	1	280-285	231,000
CB-2	2	280-285	231,000
CL	0	291 (274)	70,000 (22,000)
HL	0	325 (303)	70,000 (22,000)

which implies a direct weakness of the methodology. In this study, material retrieved from actual power plants that have been in operation have been analysed, which results in full transferability to actual plant conditions.

In this paper, austenitic weld metals from the main recirculating loops of the Swedish Ringhals unit 2 pipes that were thermally aged for 70,000 h are analysed using atom probe tomography (APT). They are compared with weld metals that have been exposed to neutron irradiation in the core barrel of the Spanish José Cabrera (Zorita) nuclear power plant. The effects of ageing on the ferrite are discussed.

2. Materials and methods

The ageing conditions of the investigated samples can be seen in Table 1. The irradiated materials originate from welds of the decommissioned José Cabrera core barrel, welded with consumables with composition consistent with type 308 [21,22]. The ferrite content of the this material was found to be 5-7%, measured by feritescope [21]. The composition of the irradiated material can be seen in Table 2. The thermally aged material is a 308-type weld from the cast material that was investigated by Bjurman et al. [23], from the reactor coolant pump elbows of Ringhals unit 2, and exhibits slightly higher ferrite content, 10±0.5% [22]. The Ringhals welds are multi-pass joints welded using Böhler EAS-2 IG (Si), a GMAW solid wire.

The samples CB-0.1 and CB-1 come from the same weld, whereas CB-2 comes from a different weld of the same component. The CL (cross-over leg) weld metal is thermally aged at a relevant temperature, 291°C, that is close to the operating temperature of the irradiated materials. The HL (hot leg) weld metal is aged at a considerably higher temperature, 325°C, resulting in an equivalent ageing of more than 10 times the CL material [22]. Both the CL and HL welds are aged 22,000 h at lower temperatures (274 and 303°C, respectively) after the initial 70,000 h. The materials are also described in an EPRI report [25].

The APT analysis was performed in a LEAP 3000X HR (Imago Scientific Instruments) equipped with a reflectron. The detection efficiency of the instrument is 37%. The analysis was done in voltage pulsed mode with a frequency of 200 kHz. The specimen temperature was 70 K, the pulse fraction was 20% and the target evaporation rate was 0.2%. Specimen preparation for APT was carried out using a standard lift-out technique ending with annular milling [26,27] in an FEI Versa 3D focused ion beam/scanning electron microscope. A final polishing at 5 kV was done in order to minimize Ga implantation and to remove any amorphous layer. Prior to the lift-out, the specimen surface was polished using oxide polishing suspension in order to make the ferrite visible.

The reconstruction was made in IVAS 3.6 (Cameca). The image compression factor was kept constant at 1.65 and the field was set to 33 V/nm. The reconstruction parameter k (field factor) was adjusted individually for each analysis containing decomposed ferrite, assuming that the extent of spinodal decomposition is isotropic (i.e. equal in z and, x and y directions). This was done by manual inspection, in combination with comparing the by Cr content normalised Cr-Cr radial distribution functions (RDFs) of some different k-value reconstructions, see the example in Fig. 1. A well-defined RDF displaying a deep minimum and a first maximum with a decreasing value for longer distances is desirable, as this should correspond to equal typical distances between the Cr-rich and Cr-poor volumes in x- y-, and z-directions. With this criterion, the k-factor was found to vary significantly between the different reconstructions, from 4.3 to 5.9. In the example in Fig. 1, k was chosen to 5.0, which gives a low minimum and at the same time a distinct local maximum.

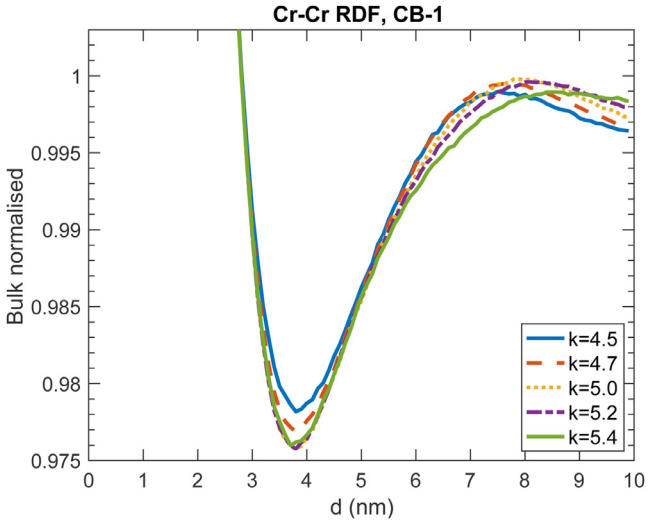

Fig. 1. Cr-Cr radial distribution functions, normalised by the Cr content of the analysis, of one of the analyses reconstructed using different k-values. The optimal value of k was regarded to be 5.0 for this measurement.

The amplitude A of the spinodal decomposition was evaluated using the Cr-Cr RDF based method by Zhou et al. [28]. The extrapolated value of the normalised Cr-Cr RDF at zero distance ($RDF(0)$) is used: $A = C_{Cr}\sqrt{RDF(0) - 1}$, where C_{Cr} is the average Cr concentration of the specific analysis. This method assumes sinusoidal concentration variations, which is a good approximation for small amplitudes in the beginning of the phase decomposition, but not as good at later stages. Independent of evaluation method, the wavelength of spinodal decomposition is dependent on the reconstruction parameters. Here, the wavelength is determined as the first local maximum of the Cr-Cr RDF. For instance, in Fig. 1, the wavelength varies between 7.5 nm and 8.6 nm depending on the k-value used, with 7.9 nm for the chosen k of 5.0. In some of the larger APT datasets (containing ferrite extending at least 150 nm), it was found that the wavelength of the spinodal decomposition could vary from the top part to the end of the reconstruction in a systematic way. When reconstructed separately, it was found that the optimum k-value varied within the analysis, and with adjusted k-value dependent on position, the difference in wavelength within the same analysis became smaller. There was, however, some remaining differences in the appearance of the RDF, mainly in the first part of the analysis where the voltage rise is the largest. These differences might be due to the need of an adjusted image compression factor as well as k, that is also known to differ during analysis, and neither of their variations are accounted for by the reconstruction algorithms used [29,30]. The impact of these effects is estimated to be small, since the k value is optimised for the average of the entire ferrite part of each analysis. Furthermore, the ferrite is in most cases not present in large parts of the reconstruction due to the narrow ferrite regions, and thus the optimised k and wavelength should be locally accurate.

Compositions from APT were deduced after careful peak deconvolution and background subtraction using IVAS 3.6. A

Table 2
The composition of the José Cabrera core barrel welds, given in wt.% and at.% [24], and the composition of the thermally aged material, measured by EDX (Mn, Cr, Fe, Ni, and Mo) and WDX (C and S). The Si contents of both materials are estimated from APT analyses of both ferrite and austenite.

	C	Mn	Si	S	Cr	Fe	Ni	Mo	Ti	Al	Cu	Co	V
CB wt%	0.06	1.47	0.85	0.017	21.5	Bal.	9.9	0.04	0.024	0.01	0.13	0.11	0.063
CB at%	0.27	1.46	1.64	0.029	22.6	Bal.	9.2	0.02	0.03	0.02	0.11	0.10	0.068
HL/CL wt%	0.017	1.65	1.00	0.008	20.6	Bal.	10.1	0.35					
HL/CL at%	0.08	1.64	1.94	0.014	21.7	Bal.	9.4	0.20					

representative mass spectrum including peak assignments can be seen in the supplementary material (Fig. S1). The APT reconstructions were analysed using both iso-concentration surfaces and proximity histograms (proxigrams) [31] and the maximum separation method (MSM) [32,33]. For the iso-concentration surfaces, a voxel size of 1 × 1 × 1 nm^3 and a delocalisation of 3 × 3 × 1.5 nm^3 nm was used. The choice of MSM parameters was carefully done, as it affects the cluster characteristics given, can be somewhat user dependent, and thus is crucial for the end results [34,35]. The parameter choice was done by comparison with randomised datasets, and solute atoms Ni, Mn and Si, $d_{max} = 0.45$ nm, and $N_{min} = 25$ were chosen. In HL and CB-0.1, the clusters were diffuse and the separation of small clusters and random fluctuations was a trade-off. For the number density, the clusters on the edges were counted as one-half. Using iso-concentration surfaces, the cluster number density was found to vary with the total Ni content of the analysis. Furthermore, many clusters did intersect each other when using iso-concentration surfaces. The MSM was found to separate closely located clusters better. The G-phase sizes were calculated using MSM, assuming only Ni, Mn and Si being part of the precipitate, the crystal structure and lattice parameter to be the same as that of the surrounding ferrite, and the detection efficiency of the instrument to be 37%. The normalisation is made as small precipitates or clusters tend to get additional matrix atoms inside due to the effect of different evaporation fields of different phases, known as local magnification [36,37]. In the example of nanometre sized Ni-Mn-Si-Cu clusters in reactor pressure vessel steels the contribution to the cluster composition from the matrix could be as high as 50% [38]. The atomic density is assumed to be close to that of the surrounding ferrite. The normalised radial concentration profiles were used to obtain the precipitate compositions, at distances where the profile is reasonably flat (0.2 to 0.5 where 1 is normalised as the cluster surface) in order to get the cluster centre composition. The enrichment of solutes in clusters is given by the cluster content divided by the average content of the analysis.

3. Results

An overview of a typical part of a CB weld can be seen in Fig. 2. The ferritic volumes are seen with a dark contrast and are surrounded by austenite. The shape of the ferrite is thin layers, with

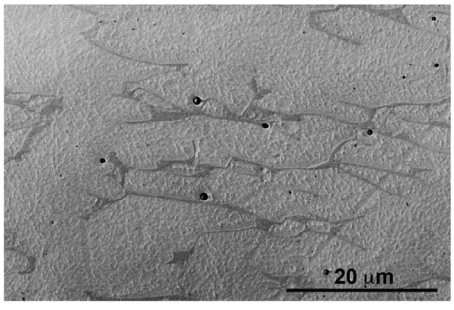

Fig. 2. Scanning electron micrograph from secondary electrons of the polished CB-2 specimen surface. The ferrite is seen as dark grey contrast.

Table 3
The composition of the analysed ferrite in the APT analyses. The standard deviations between analyses are given.

at. %	CB-0.1	CB-1	CB-2	CL	HL
C	0.03±0.04	0.07±0.03	0.06±0.05	0.05±0.01	0.02±0.01
N	0.06±0.08	0.06±0.05	0.04±0.03	0.05±0.01	0.03±0.01
Mo	0.10±0.01	0.08±0.01	0.10±0.01	0.28±0.01	0.38±0.03
Si	2.50±0.04	1.08±0.14	2.46±0.08	1.94±0.03	2.30±0.11
P	0.07±0.01	0.10±0.05	0.11±0.04	0.07±0.04	0.14±0.01
V	0.09±0.01	0.11±0.01	0.09±0.01	0.09±0.01	0.08±0.01
Mn	0.87±0.03	0.90±0.02	0.74±0.06	0.99±0.01	0.91±0.12
Cr	25.57±0.96	24.81±0.59	26.51±1.04	27.81±0.21	26.04±0.51
Co	0.06±0.01	0.05±0.01	0.05±0.01	0.13±0.08	0.12±0.01
Fe	68.22±0.89	70.87±0.96	67.32±1.37	64.25±0.14	65.83±0.33
Cu	0.04±0.01	0.03±0.01	0.03±0.01	0.08±0.01	0.08±0.01
Ni	2.33±0.07	1.77±0.29	2.42±0.22	3.39±0.04	4.01±0.20

widths as small as a few hundred nanometres. The angle of the ferrite with respect to the specimen surface is varying, some of the ferrite volumes go straight down into the material whereas others are close to parallel to the specimen surface, making the specimen preparation for APT a little more challenging. The dark spherical particles in Fig. 2 are presumably oxide inclusions that are present in the weld metal from the manufacturing.

The overall compositions of ferrite as measured by APT is given in Table 3. The compositions listed are from three analyses for each material in the case of the core barrel materials (CB-0.1, CB-1, and CB-2), and from two analyses for each material for CL and HL. The analyses come from the same lift out except in the case of CB-0.1, for which two different lift outs were made. From the standard deviations given, it is seen that the composition varies significantly between the analyses. First of all, the Cr content is different in the different analyses; for instance in the CB-2 material the Cr content varies between 25.3 and 27.3 at.%. There is also a significant spread among the analyses of irradiated material, but also between the irradiated materials and the thermally aged materials in terms of the Ni content. Furthermore, the Si content of material CB-1 is considerably lower (0.9-1.2%) than in the other materials (1.9-2.5%). The differences between thermally aged and irradiated material might be partly due to differences during manufacturing, for instance in the cooling rate, that will influence the kinetics and thus the partitioning of elements between the ferrite and the austenite. There could also be overall differences in the compositions between the welds. On top of that, there seems to be local differences within the composition that are caught due to the local analysis of APT, probably due to the complex structure. The ferrite composition might vary between different grains. Within the same APT reconstruction, the ferrite composition was found to be fairly constant, also in the vicinity of ferrite/austenite boundaries.

Thin slices of the ferrite of all five materials studied can be seen in Fig. 3, where volumes of 20 × 20 × 4 nm^3 are presented. The spinodal decomposition of the materials is visualized by only displaying the distribution of Cr atoms. In CL, no spinodal decomposition is seen. In HL, there are some small Cr density variations within the ferrite. In all irradiated materials, on the other hand, the phase separation is clear and the difference between CB-0.1, CB-1 and CB-2 is small. The difference between CB-1 and CB-2

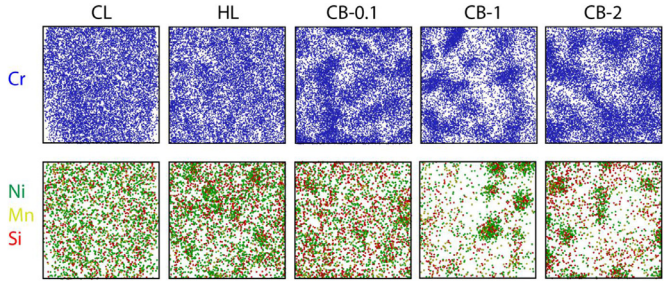

Fig. 3. Thin slices (thickness 4 nm) of APT analyses showing the distribution of Cr and Ni, Mn and Si in the ferrite for all different conditions. The sides of the boxes are 20 nm. The decreased Cr content in the bottom corners of the CL image is due to the ferrite volume being too small to fill the 20 × 20 × 4 nm^3 box, leaving the corners outside the reconstruction.

regarding spinodal decomposition is as small as the variation within the same ageing condition.

Also in Fig. 3, the distribution of Ni, Mn and Si is seen for the same volumes. Again, the distribution appears to be random in CL. In HL and CB-0.1, clusters have started to form, whereas in CB-1 and CB-2, the G-phase precipitates are well developed and can be clearly separated from the matrix. In this study, we have no crystallographic information on the clusters as APT is used, but the words *precipitate* and *phase* are still used.

3.1. Spinodal decomposition

The spinodal decomposition of all analyses was evaluated in terms of wavelength and amplitude, using the Cr-Cr RDFs in Fig. 4a). The proxigrams of Cr are shown in Fig. 4b). In both the RDFs and the proxigrams it is clear that there is a phase decomposition into Cr-rich and Cr-poor volumes in the materials. Looking at both RDFs and proxigrams, the CB-1 and CB-2 materials overlap and show high degrees of decomposition, the CB-0.1 material shows almost as much phase decomposition, and the thermally aged HL material shows less fluctuations in the Cr content than any of the irradiated materials. CL shows no signs of decomposition.

The wavelength as a function of local Cr concentration (Cr concentration of the specific analysis) of all materials, except CL, can be seen in Fig. 5. When comparing the wavelength with the measured Cr concentration of each analysis, there is a trend for a longer wavelength with higher Cr for the irradiated materials, and possibly the same trend is present also for unirradiated material,

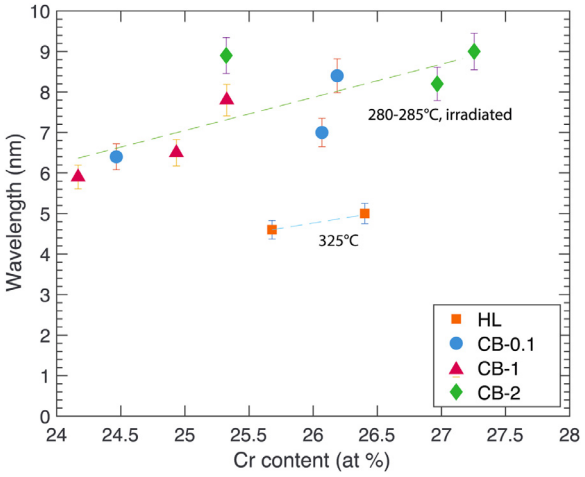

Fig. 5. Wavelength vs local Cr concentration of the materials except CL. The thermally aged material included, the HL weld, was aged at a higher temperature (325°C), than the irradiated materials (280-285°C). Error bars are estimated from the possible difference in wavelength from reasonable values of the reconstruction parameters.

but at shorter wavelengths. The relation between wavelength and dose is not clear, as CB-1 has a shorter average wavelength than the CB-0.1 material, and the wavelength of one of the analyses of CB-0.1 was longer than the wavelength of one of the analyses of CB-2. The measurement error is estimated to be smaller (it is estimated to be less than ±0.5 nm based on the reasoning in the methods section) than the variation between the various analyses of the same materials.

The amplitude of the spinodal decomposition, calculated as described above, shows a small increase from CB-0.1 to CB-1, see Fig. 6. Materials CB-1 and CB-2 appear to have similar amplitudes of around 25 at.%. Material HL has a lower amplitude, 14 at.%, and CL is not included in the figure as there is no clear spinodal decomposition. The influence of local composition on the amplitude has no obvious trend and is hence not shown. A full comparison of amplitude and wavelength can be seen in Fig. 7. The spinodal decomposition in the irradiated materials is much more developed than in the thermally aged HL, although the temperature during irradiation was lower. It appears to be only small differences between CB-1 and CB-2 that might be due to the composition, mainly the Cr content, of the ferrite in each individual grain. Already

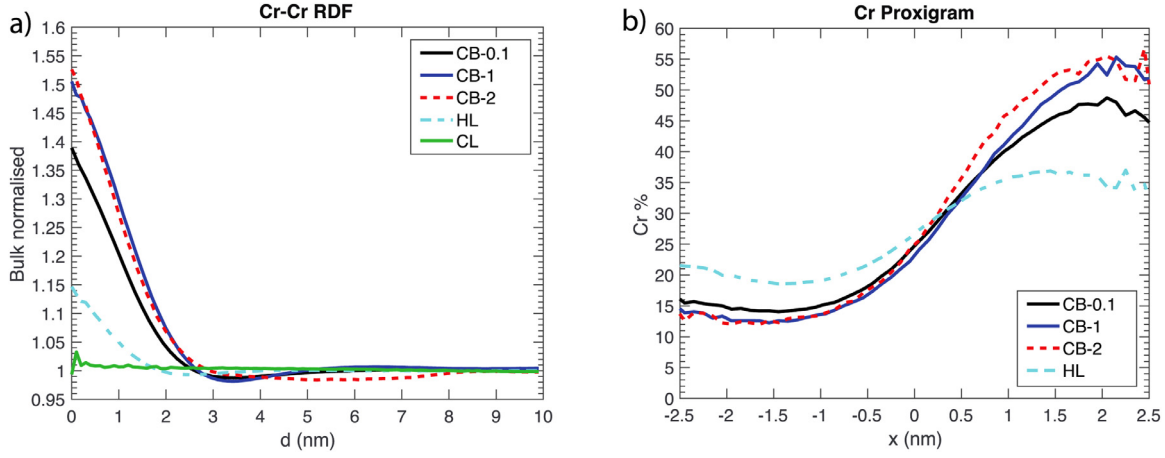

Fig. 4. a) Cr-Cr radial distribution functions for one representative analysis of every material. All materials except CL display spinodal decomposition. b) Representative proxigrams around the average Cr value for each material, except CL, are also shown. For the curves of all analyses, the reader is referred to the supplementary material (Figure S2).

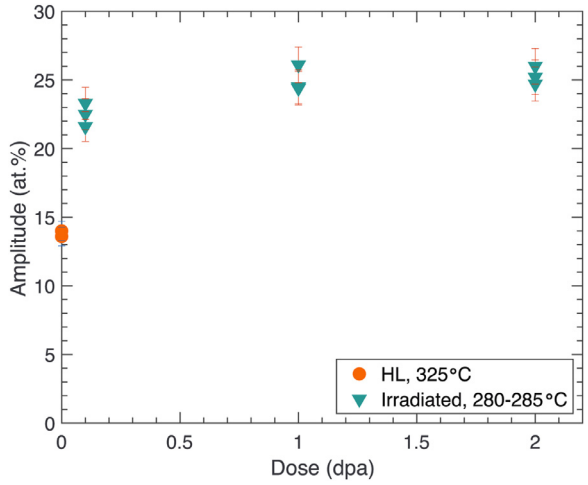

Fig. 6. Amplitude of the spinodal decomposition as a function of dose. The thermally aged material included, the HL weld, is aged at a higher temperature (325°C), than the irradiated materials (280-285°C). The relative error of the amplitude is estimated to 5%.

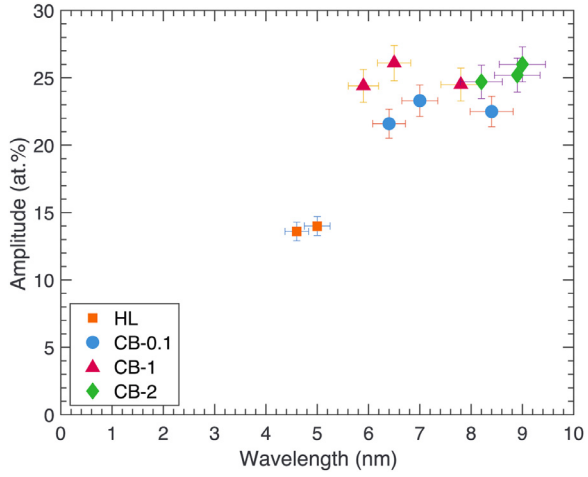

Fig. 7. A summary of the amplitude and wavelength for the spinodally decomposed ferrite. The thermally aged material included, HL, is aged at a higher temperature (325°C) than the irradiated materials (280-285°C).

after irradiation to 0.1 dpa the spinodal decomposition is well developed.

3.2. G-phase formation

The absolute Ni-Ni RDFs of all materials are shown in Fig. 8. In all materials except CL, Ni is found to cluster (Mn and Si also cluster with Ni, but this is not shown in the figure), indicating formation of G-phase. The absolute RDFs are shown rather than the normalised RDFs, so that the effect of Ni content can also be seen, as the Ni is varying significantly between the materials. The difference in Ni content does not seem to significantly affect the cluster composition, and thus the values at small distances end up closer to each other when not normalised to the bulk content. From Fig. 8 it can be seen that the RDFs of Ni in CB-1 and CB-2 are considerably higher than for CB-0.1, and they are overlapping, indicating a possible saturation of Ni clustering with respect to dose, occurring at a dose below 1 dpa. The HL and CL materials have higher ferrite Ni content (also shown in Table 3). In the CL material, no apparent clustering is indicated by the RDF.

The composition of the G-phase precipitates found in all materials except CL was analysed using the MSM and the results are

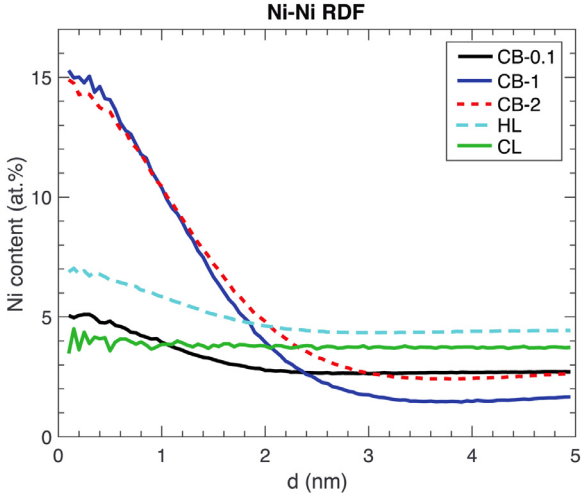

Fig. 8. The absolute Ni-Ni RDFs for the ferrite of all materials, with one representative analysis per material. All Ni-Ni RDFs are shown in the supplementary material (Figure S3).

presented in Fig. 9. Here, both the absolute content and a normalised composition (only Ni, Mn, and Si) for comparison to the stochiometric $Ni_{16}Si_7Mn_6$ G-phase composition are shown. The Mn content is in general a bit lower than expected from the stoichiometry, whereas the Si content is higher. The Mn and Ni might be replaced by Fe or Cr in the G-phase, which were removed from the precipitate content in the normalisation. The materials show similar G-phase compositions, as is expected in the case of the precipitates being the same phase.

The enrichment of Ni, Mn, Si, P and Cu in the clusters is shown in Fig. 10. Most of the irradiated materials show similar enrichment factors of the solutes. The analysis of CB-1 that has high enrichments has similar cluster composition, but low total contents and thus low matrix contents, giving the high enrichment. HL has similar or slightly lower enrichments of all solutes except P, which clearly becomes less enriched after thermal ageing than after irradiation. The total Cu content of the ferrite is low (0.03-0.08 at%), and thus even the high enrichment factors of 5-15 result in a low total precipitate Cu content.

The average G-phase diameter for the CB-1 and CB-2 materials was found to be around 2 nm, with distributions ranging from 1 to 3 nm. Hereby any Fe and Cr atoms inside clusters were removed (assuming they were detected inside clusters due to local magnification effects), thus possibly underestimating the size. In the HL and CB-0.1 material, the clusters are more diffuse and thus harder to define. In general, applying MSM on HL and CB-0.1 results in a smaller number of atoms in the clusters in these materials, but the results are very much dependent on the MSM parameter choice and a very sharp cut-off in the size distribution occurs due to the N_{min} parameter, indicating that the MSM is not a suitable technique to quantify these diffuse features.

The G-phase number densities were found to be high, between 1.5-4.5 $10^{24}/m^3$. For HL the average was 3.6 $10^{24}/m^3$, for CB-0.1 2.5 $10^{24}/m^3$, for CB-1 2.5 $10^{24}/m^3$, and for CB-2 4.3 $10^{24}/m^3$, thus with a weak increasing trend with dose, but below that trend for CB-1 that also contains less Ni.

4. Discussion

In this study we have found significant microstructural changes that are attributed to the neutron irradiation and thermal ageing of the material, in the ferrite phase.

In the CL material, no apparent spinodal decomposition was found to take place after thermal ageing for 70,000 h. CL is a

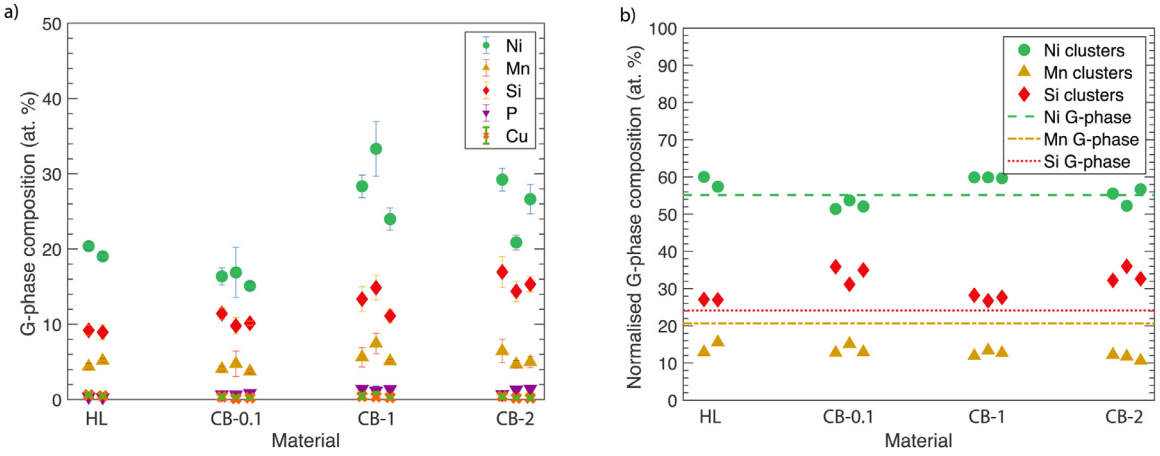

Fig. 9. a) G-phase composition for materials HL, CB-0.1, CB-1 and CB-2. Error bars given reflect the standard deviation of the data points in the normalised radial concentration profiles that were used for the composition determination. b) The normalised contents are shown and compared to stoichiometric G-phase composition. The thermally aged material included, the HL weld, is aged at a higher temperature (325°C), than the irradiated materials (280-285°C).

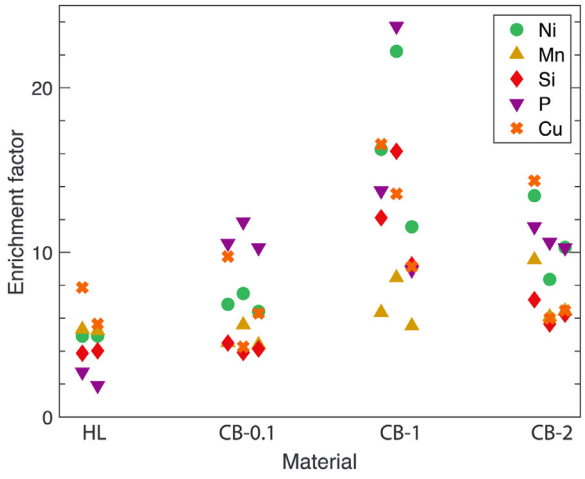

Fig. 10. Enrichment factors (relative to the matrix) of Ni, Mn, Si, P, and Cu in the G-phase, for material HL, CB-0.1, CB-1 and CB-2. The thermally aged material included, the HL weld, is aged at a higher temperature (325°C), than the irradiated materials (280-285°C).

relevant comparison and reference to the irradiated materials, as the ageing temperature of 291°C is only slightly higher than the 280-285°C that is the temperature experienced by the irradiated materials. The equivalent ageing can, assuming 281°C for the irradiated core barrel welds, and using the Arrhenius equation with an activation energy of 243 kJ/mol, be calculated for CL and HL to 188,000 h and 3,590,000 h, respectively [39]. Comparing the results of the CL weld and the irradiated materials, that then should have similar equivalent ageing times in terms of thermal ageing, it is obvious that the neutron irradiation is central in the degradation of the materials, as CL shows no degradation in terms of spinodal decomposition and G-phase formation. The degree of spinodal decomposition, in terms of both wavelength and amplitude, seems to be almost independent of dose (in the range of 0.1-2 dpa), but there is an effect of the local Cr concentration. The observation that a higher Cr content speeds up the decomposition is expected [28]. Miller et al. studied a Fe-32%Cr model alloy, that was neutron irradiated to 0.06 dpa, and compared to thermal ageing of the same material [19]. The neutron irradiation played a major role in the decomposition of this alloy, in correspondence with the results obtained here.

The slightly different compositions of the materials might influence the spinodal decomposition. For instance, the higher Ni content of the thermally aged CL and HL (3.4-4.0 at.% as compared to 1.8-2.4 at.% in the irradiated materials) might influence the decomposition, as seen by Zhou et al. [40]. However, a higher Ni content is expected to give a faster spinodal decomposition, and thus, the effect of neutron irradiation is larger than the effect of the difference in Ni content in the materials studied in this paper.

The dose rate was the highest in CB-2, but it was low in comparison to accelerated experiments and magnitudes below dose rates where ballistic mixing is to be expected [41]. The Cr content of the α phase of material CB-1 and CB-2 is 10-12 at.% (Fig. 4). This is close to the thermodynamically stable 9-10% in a binary Fe-Cr model alloy [42,43], although the actual composition of the alloy might impact the equilibrium Cr content. This makes it probable that the α phase has reached a steady state equilibrium after 1 dpa (and probably at even lower doses, as even the CB-0.1 material is close to saturation). In the α' phase, the Cr content is around 50% in CB-1 and CB-2. This is not saturated according to phase diagrams, but this might be due to the α/α' interfacial energy being low, thus not pushing the coarsening of α' [5].

The G-phase was found to be more well-developed in CB-1 and CB-2 than in CB-0.1 and HL. Thus, the degree of G-phase formation is the largest difference between CB-0.1 and the materials irradiated to higher doses, as the spinodal decomposition appears to be close to saturation already in the CB-0.1 material. In CL, no G-phase precipitation was observed. The reason why the G-phase number density is lower after irradiation to 1 dpa than 2 dpa is probably at least partly due to the considerably lower Ni and Si content in the CB-1 material analysed.

It is interesting to note that the G-phase precipitation is similar in the HL material and the CB-0.1 material, in terms of absolute increase in the non-normalised Ni-RDFs (Fig. 8) and the enrichment of solute elements (Fig. 10), although the difference in spinodal decomposition is obvious, HL has considerably smaller amplitude and wavelength (Fig. 7). In general, the G-phase nucleation is assumed to be strongly connected with the spinodal decomposition, by the rejection of Ni from the α phase, and Mn and Si from the α'. There are a number of possible explanations for the phenomena observed here. It could be that the fundamental difference between thermal ageing and neutron irradiation makes the difference. It could be that the G-phase evolves gradually, but first to the state that we see in both HL and CB-0.1, and then requires much more diffusion to evolve to what is seen in CB-1 and CB-2. APT does not give any crystallographic information, and thus it is possible that the agglomeration of Ni, Mn and Si that we see has not yet transformed into G-phase precipitates in HL and CB-0.1, possibly due to too high Fe-content [44]. It could also be the slightly different composition (higher Ni and Mo content of the ferrite) that speeds

up the G-phase formation in HL. Mo is known to increase G-phase formation, for instance Pareige et al. [45] observed a difference in G-phase precipitation in ferrite containing Mo and Mo-free ferrite. However, the Mo concentration differences were significantly larger than in this case (0.04 wt.% was compared with 2.5 wt.%, corresponding to almost 5 at.%, to compare with the difference between 0.1 at.% and 0.4 at.% in this paper). At this moment, it is unclear what mechanisms are the main responsible ones.

4.1. Influence of the microstructure on mechanical properties

The question of the impact of the microstructure on the mechanical properties is complex, due to the many different degradation modes in the material. Spinodal decomposition is known to affect the mechanical properties of duplex steels. The influence of G-phase formation is debated, with some results suggesting that it does affect the properties marginally and some that it does significantly impact the mechanical properties [5,12]. There is also a possibility of an indirect dependence due to the changed composition of the ferrite surrounding the G-phase precipitates, that in turn affects the spinodal decomposition [5,11].

In the irradiated materials, the ferrite is not continuous, forcing any propagating cracks to transition through austenite. Furthermore, the ferrite constitutes only 5-7% of the total volume, thus changes in the austenite are inevitably important for the mechanical properties. In the austenite of the irradiated materials, Ni-Si precipitates are expected to be found to varying extent [46]. These make the material harder and might also make the material embrittled [47]. In addition to the precipitates, loops (decorated with Ni and Si), as well as matrix defects are probably formed during irradiation, which also have a significant effect on the mechanical properties [48,49].

The effect of irradiation on mechanical properties and in particular fracture toughness is in contrast to the APT data of the ferrite in this study not saturated below 1 dpa and further degradation occurs in the 1-10 dpa interval [50]. It is known that the irradiated José Cabrera materials show significant irradiation hardening and reduction in fracture toughness in the dose span investigated here [24]. The effects of irradiation on the austenite and on the ferrite/austenite phase boundaries and the influence of the different degradation mechanisms on mechanical properties are the subject of an ongoing study.

5. Conclusions

Both welds irradiated up to 2 dpa over a period of 231,000 h and thermally aged welds (70,000 h at 291 and 325°C) have been studied. In general, the difference between irradiation of the weld material to 1 and 2 dpa was small. It was found that:

- The spinodal decomposition of the ferrite was almost saturated after neutron irradiation to 0.1 dpa. There were no significant differences between the materials irradiated to 1 and 2 dpa regarding the decomposition. The wavelengths were 6-9 nm irrespective of dose. The Cr amplitudes were found to be 21-24 at.%, 24-26 at. % and 24-26 at.% for CB-0.1, CB-1 and CB-2, respectively.
- The spinodal decomposition was more developed in grains with higher Cr content, with a linear relationship between wavelength and Cr concentration.
- Thermal ageing at 291°C (the CL material) was not enough for spinodal decomposition to develop. However, thermal ageing at 325°C for the same time (the HL material) significantly changed the Cr and Fe distributions in the ferrite, giving spinodal decomposition with a wavelength of 5 nm and Cr amplitude of 13-14 at.%.
- Care needs to be taken when reconstructing the APT datasets for evaluation of spinodal decomposition, especially for the wavelength measurements.
- G-phase was found in the HL, CB-0.1, CB-1 and CB-2 materials, with number density in the range 1.5-4.5 10^{24} m^{-3}. There is a significant difference between CB-0.1, on one hand, and CB-1 and CB-2, on the other, with larger (2 nm in diameter) and more well defined G-phase precipitates after higher dose. The composition of the G-phase is close to the nominal $Ni_{16}Si_7Mn_6$.

Declaration of Competing Interest

The authors declare that they have no known competing financial interests or personal relationships that could have appeared to influence the work reported in this paper.

CRediT authorship contribution statement

K. Lindgren: Investigation, Formal analysis, Visualization, Conceptualization, Writing – original draft, Writing – review & editing. **M. Bjurman:** Funding acquisition, Conceptualization, Writing – review & editing. **P. Efsing:** Funding acquisition, Conceptualization, Supervision, Writing – review & editing. **M. Thuvander:** Conceptualization, Supervision, Writing – review & editing.

Acknowledgments

EPRI is thanked for funding and contributing with the irradiated materials. Furthermore, the Swedish Radiation Safety Authority (SSM) is acknowledged for funding, and Ringhals for providing the thermally aged weld metals. Peter Ekström at the Swedish Safety Authority (SSM) is acknowledged for good discussions. This work was performed in part at the Chalmers Materials Analysis Laboratory, CMAL.

Supplementary materials

Supplementary material associated with this article can be found, in the online version, at doi:10.1016/j.jnucmat.2021.152967.

References

[1] H.M. Chung, Aging and life prediction of cast duplex stainless steel components, Int. J. Press. Vessels Pip. 50 (1992) 179–213.
[2] A. Pineau, J. Besson, Thermal embrittlement of cast duplex stainless steels: observations and modeling, in: I. Alvarez-Armas, S. Degallaix-Moreuil (Eds.), Duplex Stainless Steels, John Wiley & Sons, Inc., 2013.
[3] T. Wegrzyn, Delta ferrite in stainless steel weld metals, Weld. Int. 6 (9) (1992) 690–694.
[4] TBM- technical regulations for mechanical equipment, Swedish Nucl. Power Companies (2015).
[5] F. Danoix, P. Auger, Atom probe studies of the Fe–Cr system and stainless steels aged at intermediate temperature: a review, Mater. Charact. 44 (1–2) (2000) 177–201.
[6] K.H. Lo, C.H. Shek, J.K.L. Lai, Recent developments in stainless steels, Mater. Sci. Eng. 65 (4–6) (2009) 39–104.
[7] A. Mateo, L. Llanes, M. Angelada, A. Redjaimia, G. Metauer, Characterization of the intermetallic G-phase in an AISI 329 duplex stainless steel, J. Mater. Sci. 32 (1997) 4533–4540.
[8] J. Bentley, M.K. Miller, S.S. Brenner, J.A. Spitznagel, Identification of G-phase in aged cast CF8 type stainless steel, in: G.W. Bailey (Ed.), Annual Meeting of the Electron Microscopy Society of America, 1985, pp. 328–329.
[9] M.K. Miller, J. Bentley, APFIM and AEM investigation of CF8 and CF8M primary coolant pipe steels, Mater. Sci. Technol. 6 (3) (1990) 285–292.
[10] C. Pareige, S. Novy, S. Saillet, P. Pareige, Study of phase transformation and mechanical properties evolution of duplex stainless steels after long term thermal ageing (>20years), J. Nucl. Mater. 411 (1–3) (2011) 90–96.
[11] H.M. Chung, T.R. Leax, Embrittlement of laboratory and reactor aged CF3,CF8, and CF8M duplex stainless steels, Mater. Sci. Technol. 6 (3) (1990) 249–262.
[12] W. Guo, D.A. Garfinkel, J.D. Tucker, D. Haley, G.A. Young, J.D. Poplawsky, An atom probe perspective on phase separation and precipitation in duplex stainless steels, Nanotechnology 27 (25) (2016) 254004.

[13] T. Hamaoka, A. Nomoto, K. Nishida, K. Dohi, N. Soneda, Accurate determination of the number density of G-phase precipitates in thermally aged duplex stainless steel, Philos. Mag. 92 (22) (2012) 2716–2732.
[14] T.G. Lach, A. Devaraj, K.J. Leonard, T.S. Byun, Co-dependent microstructural evolution pathways in metastable δ-ferrite in cast austenitic stainless steels during thermal aging, J. Nucl. Mater. 510 (2018) 382–395.
[15] P. Hedström, F. Huyan, J. Zhou, S. Wessman, M. Thuvander, J. Odqvist, The 475°C embrittlement in Fe–20Cr and Fe–20Cr–X (X=Ni, Cu, Mn) alloys studied by mechanical testing and atom probe tomography, Mater. Sci. Eng. 574 (2013) 123–129.
[16] K. Fujii, K. Fukuya, Effects of radiation on spinodal decomposition of ferrite in duplex stainless steel, J. Nucl. Mater. 440 (1–3) (2013) 612–616.
[17] O.A. Korchuganova, M. Thuvander, A.A. Aleev, S.V. Rogozhkin, T. Boll, T.V. Kulevoy, Microstructural evolution of Fe22%Cr model alloy under thermal ageing and ion irradiation conditions studied by atom probe tomography, J. Nucl. Mater. 477 (2016) 172–177.
[18] S. Chen, Y. Miyahara, A. Nomoto, K. Nishida, Effects of thermal aging and low-fluence neutron irradiation on the mechanical property and microstructure of ferrite in cast austenitic stainless steels, Acta Mater. 179 (2019) 61–69.
[19] M.K. Miller, R.E. Stoller, K.F. Russell, Effect of neutron-irradiation on the spinodal decomposition of Fe-32% Cr model alloy, J. Nucl. Mater. 230 (1996) 219–225.
[20] T.S. Byun, Y. Yang, N.R. Overman, J.T. Busby, Thermal aging phenomena in cast duplex stainless steels, Jom 68 (2) (2015) 507–516.
[21] M. Bjurman, K. Lindgren, M. Thuvander, P. Ekström, P. Efsing, Microstructural evolution of welded stainless steels on integrated effect of thermal aging and low flux irradiation, in: J.H. Jackson, D. Paraventi, M. Wright (Eds.), the 18th International Conferece on Environmental Degradation of Materials in Nucler Power Systems - Water Reactors, Springer, 2018, pp. 703–710.
[22] M. Bjurman, M. Thuvander, K. Lindgren, P. Efsing, Thermal aging and irradiation of cast and welded stainless steels and the influence on LTO, Fontevraud 9, Avignon, 2018.
[23] M. Bjurman, M. Thuvander, F. Liu, P. Efsing, Phase separation study of in-service thermally aged cast stainless steel – atom probe tomography, 17th International Conference on Environmental Degradation of Materials in Nuclear Power Systems – Water Reactors, 2015.
[24] A. Jenssen, J. Stjärnsäter, K. Kese, R. Carter, J. Smith, A. Demma, M. Hiser, Fracture toughness testing of an irradiated PWR core barrel weld, Fontevraud 9, Avignon (2018).
[25] Materials Reliability Program: Thermal Aging Analysis of Stainless Steel Weld Material at High and Low Neutron Irradiation Dose (MRP-441), EPRI, Palo Alto, CA, 2019.
[26] D.J. Larson, D.T. Foord, A.K. Petford-Long, H. Liew, M.G. Blamire, A. Cerezo, G.D.W. Smith, Field-ion specimen preparation using focused ion-beam milling, Ultramicroscopy 79 (1–4) (1999) 287–293.
[27] K. Thompson, D. Lawrence, D.J. Larson, J.D. Olson, T.F. Kelly, B. Gorman, In situ site-specific specimen preparation for atom probe tomography, Ultramicroscopy 107 (2–3) (2007) 131–139.
[28] J. Zhou, J. Odqvist, M. Thuvander, P. Hedstrom, Quantitative evaluation of spinodal decomposition in Fe-Cr by atom probe tomography and radial distribution function analysis, Microsc. Microanal. 19 (3) (2013) 665–675.
[29] F. Vurpillot, B. Gault, B.P. Geiser, D.J. Larson, Reconstructing atom probe data: a review, Ultramicroscopy 132 (2013) 19–30.
[30] B. Gault, S.T. Loi, V.J. Araullo-Peters, L.T. Stephenson, M.P. Moody, S.L. Shrestha, R.K. Marceau, L. Yao, J.M. Cairney, S.P. Ringer, Dynamic reconstruction for atom probe tomography, Ultramicroscopy 111 (11) (2011) 1619–1624.
[31] O.C. Hellman, J.A. Vandenbroucke, J. Rüsing, D. Isheim, D.N. Seidman, Analysis of three-dimensional atom-probe data by the proximity histogram, Microsc. Microanal. 6 (5) (2000) 437–444.
[32] J.M. Hyde, C.A. English, An analysis of the structure of irradiation induced cu-enriched clusters in low and high nickel welds, Materials Research Society Symposium, 2000 pp. R6.6.1-R6.6.12.
[33] D. Vaumousse, A. Cerezo, P.J. Warren, A procedure for quantification of precipitate microstructures from three-dimensional atom probe data, Ultramicroscopy 95 (2003) 215–221.
[34] Y. Dong, A. Etienne, A. Frolov, S. Fedotova, K. Fujii, K. Fukuya, C. Hatzoglou, E. Kuleshova, K. Lindgren, A. London, A. Lopez, S. Lozano-Perez, Y. Miyahara, Y. Nagai, K. Nishida, B. Radiguet, D.K. Schreiber, N. Soneda, M. Thuvander, T. Toyama, J. Wang, F. Sefta, P. Chou, E.A. Marquis, Atom probe tomography interlaboratory study on clustering analysis in experimental data using the maximum separation distance approach, Microsc. Microanal. 25 (2) (2019) 356–366.
[35] K. Lindgren, K. Stiller, P. Efsing, M. Thuvander, On the analysis of clustering in an irradiated low alloy reactor pressure vessel steel weld, Microsc. Microanal. 23 (2) (2017) 376–384.
[36] M.K. Miller, R.G. Forbes, Atom-Probe Tomography: The Local Electrode Atom Probe, Springer, New York, 2014.
[37] E.A. Marquis, J.M. Hyde, Applications of atom-probe tomography to the characterisation of solute behaviours, Mater. Sci. Eng. 69 (4–5) (2010) 37–62.
[38] K. Lindgren, M. Boåsen, K. Stiller, P. Efsing, M. Thuvander, Evolution of precipitation in reactor pressure vessel steel welds under neutron irradiation, J. Nucl. Mater. 488 (2017) 222–230.
[39] M. Bjurman, B. Forssgren, P. Efsing, Fracture mechanical testing of in-service thermally aged cast stainless steel, in: Z. Wei, P.C. McKeighan, D.G. Harlow (Eds.), Fatigue and Fracture Test Planning, Test Data Acquisitions and Analysis, ASTM STP1598, ASTM international, West Conshohocken, PA, 2017, pp. 58–80.
[40] J. Zhou, J. Odqvist, M. Thuvander, S. Hertzman, P. Hedström, Concurrent phase separation and clustering in the ferrite phase during low temperature stress aging of duplex stainless steel weldments, Acta Mater. 60 (16) (2012) 5818–5827.
[41] F. Soisson, E. Meslin, O. Tissot, Atomistic modeling of α' precipitation in Fe-Cr alloys under charged particles and neutron irradiations: effects of ballistic mixing and sink densities, J. Nucl. Mater. 508 (2018) 583–594.
[42] M. Bachhav, G.Robert R. Odette, E.A. Marquis, α' precipitation in neutron-irradiated Fe–Cr alloys, Scr. Mater. 74 (2014) 48–51.
[43] W. Xiong, P. Hedström, M. Selleby, J. Odqvist, M. Thuvander, Q. Chen, An improved thermodynamic modeling of the Fe–Cr system down to zero kelvin coupled with key experiments, Calphad 35 (3) (2011) 355–366.
[44] D.J.M. King, P.A. Burr, S.C. Middleburgh, T.M. Whiting, M.G. Burke, M.R. Wenman, The formation and structure of Fe-Mn-Ni-Si solute clusters and G-phase precipitates in steels, J. Nucl. Mater. 505 (2018) 1–6.
[45] C. Pareige, J. Emo, S. Saillet, C. Domain, P. Pareige, Kinetics of G-phase precipitation and spinodal decomposition in very long aged ferrite of a Mo-free duplex stainless steel, J. Nucl. Mater. 465 (2015) 383–389.
[46] A. Etienne, B. Radiguet, P. Pareige, J.P. Massoud, C. Pokor, Tomographic atom probe characterization of the microstructure of a cold worked 316 austenitic stainless steel after neutron irradiation, J. Nucl. Mater. 382 (1) (2008) 64–69.
[47] E.A. Kenik, J.T. Busby, Radiation-induced degradation of stainless steel light water reactor internals, Mater. Sci. Eng. 73 (7–8) (2012) 67–83.
[48] C. Pokor, Y. Brechet, P. Dubuisson, J.P. Massoud, X. Averty, Irradiation damage in 304 and 316 stainless steels: experimental investigation and modeling. Part II: irradiation induced hardening, J. Nucl. Mater. 326 (1) (2004) 30–37.
[49] C. Pokor, Y. Brechet, P. Dubuisson, J.P. Massoud, A. Barbu, Irradiation damage in 304 and 316 stainless steels: experimental investigation and modeling. Part I: evolution of the microstructure, J. Nucl. Mater. 326 (1) (2004) 19–29.
[50] O.K. Chopra, A.S. Rao, A review of irradiation effects on LWR core internal materials - neutron embrittlement, void swelling, and irradiation creep, NRC report ML102010621, 2010.